Computational Fluid Dynamics Analysis of the Stall Characteristics of a Wing Designed Based on Prandtl's Minimum Induced Drag

Seung Y. Yoo[1]
NASA Armstrong Flight Research Center, Edwards, CA 93523

Stall characteristics of a wing designed based on Prandtl's minimum induced drag solution using the bending moment as the design constraint is presented. The flow field is resolved using the Reynold-Averaged Navier Stokes solver OVERFLOW, version 2.2*l*, with fully turbulent flow approximation. The turbulence was resolved using the Spalart-Allmaras turbulence model with rotational and curvature correction. Grid independence study shows acceptable grid resolution is achieved. The stall angle of attack was predicted at 17.25°. Computational fluid dynamics analysis shows that large separations begin inboard, near the symmetry plane, and exist at stall. However, the separated region remains localized, and the flow at the wing tip remains attached.

I. Nomenclature

AIAA = American Institute of Aeronautics and Astronautics
AoA = angle of attack
CAD = computer aided design
CFD = computational fluid dynamics
CGT = Chimera Grid Tools
C_D = drag coefficient
C_L = lift coefficient
C_m = pitching moment coefficient
C_P = pressure coefficient
i = automatically generated far field grid level
MAC = mean aerodynamic chord
MSL = mean sea level
NASA = National Aeronautics and Space Administration
PRANDTL-D = Preliminary Research Aerodynamic Design To Lower Drag
RANS = Reynolds-Averaged Navier-Stokes
x, y, z = Cartesian coordinate, origin at the leading edge, wing symmetry plane
y+ = nondimensional wall distance

Subscript
MRC = moment reference center

II. Introduction

Computational fluid dynamics (CFD) analysis of the stall characteristic of a wing design based on Prandtl's minimum induced drag result [1] is presented. The aerodynamic flow associated with a three dimensional, medium to high aspect ratio wing at a large angle of attack is complex. The complexity is emphasized especially in the proximity of maximum lift and stall, recognized by a sharp break in lift over angle of attack. Some of the flow features that contribute to the complexity are intricate wake features, wake / boundary layer merging, regions of flow separation, laminar-to-turbulent transition regions, et cetera [2]. As such, one of the major focuses in the current research field is

---

[1] Aerospace engineer, Controls and Dynamics Branch, P.O. Box 273/MS 4840D, Edwards California, 93523-0273, non-member.

the accurate simulation and prediction of the flow physics at such a condition. The prime example of such an effort is the American Institute of Aeronautics and Astronautics (AIAA) High Lift Prediction Workshop [2-4]. The workshop determines the current state-of-the-art numerical simulation capability by comparing the CFD simulation results against extensive wind-tunnel experiment data. Results have shown that flow physics in the region of stall and maximum lift are highly sensitive to the numerical schemes and turbulence models utilized. Wide spread of CFD results were observed at the stall region for various solvers and turbulence models for all workshops held to date. No clear trend was observed for any specific turbulence model utilized. Although some CFD results matched well against the wind-tunnel data, the general conclusion was that the best practice should be formulated for individual solvers.

In recent years, intense CFD simulations were performed at the National Aeronautics and Space Administration (NASA) Armstrong Flight Research Center (Edwards, California) on the NASA modified Gulfstream Aerospace Corporation (Savannah, Georgia) Gulfstream-III aircraft. The study was conducted in a systematic manner while using the best practices developed to produce consistent solutions. The goal was to capture and predict the flow of the modified aircraft [5, 6] at stall. The results were critical in determining safe test conditions. The study presented in this paper presents the analysis of the behavior of the flow near the stall region of a wing that was designed [7] based on Prandtl's work [1]. The analysis was conducted using CFD, solving the Reynolds-Averaged Navier-Stokes (RANS) equation using the OVERFLOW [8] flow solver. Simulations were conducted following the best-practices [9, 10] developed for the solver. Some of the best practices utilized are listed below.

1) The surface and volume grid stretching ratio should be less than 1.25.
2) Neighboring grids should have a minimum of 5 points overlap for second order overset interpolation.
3) The cell spacing normal to the viscous wall should be constant for at least the first two cells.
4) The initial y+ value should be less than 1.0.
5) High angle of attack simulation should start from the lower angle of attack solution to prevent early stall that may result due to numerical hysteresis.
6) The Spalart-Allmaras turbulence model with rotational and curvature correction should be used to model turbulence.

This paper is organized as following. Section III presents the aircraft details and briefly summarizes Prandtl's theory that was used to design the wing. Section IV provides the simulation details such as the atmospheric condition, solver settings, and mesh generation settings. The simulation results and the associated discussions are provided in section V. The results include the grid independence study and the flow analysis. This paper will conclude with a summary of the work presented.

III. Aircraft

The aircraft analyzed is designated as P-3C under the Preliminary Research AerodyNamic Design To Lower Drag (PRANDTL-D) program at NASA Armstrong Flight Research Center [7]. The aircraft is a remotely piloted aircraft with a wingspan of 24.6 feet and a cruising speed of approximately 30 feet per second. A picture of the aircraft is shown in Fig. 1. Several simplifications were made to the aircraft outer-mold-line for simulation purposes. Control surfaces and the actuator mechanisms were not modeled. The protrusions due to instrumentation were also not included in the simulation model. The computer aided design (CAD) model used in the simulation is shown in Fig. 2. The reference quantities such as the mean aerodynamic chord (MAC), planform area, and span are tabulated in Table 1. The coordinate of the moment reference center, also provided in Table 1, is given with respect to the origin placed at the nose of the vehicle at the symmetry plane.

Table 1. Reference quantities.

Variable	Value	Unit
Planform area	40.5	ft^2
Mean aerodynamic chord	1.969	ft
Span	24.6	ft
x_{MRC}, y_{MRC}, z_{MRC}	2.125, 0.0, -0.196	ft

Fig. 1. P-3C aircraft in flight.

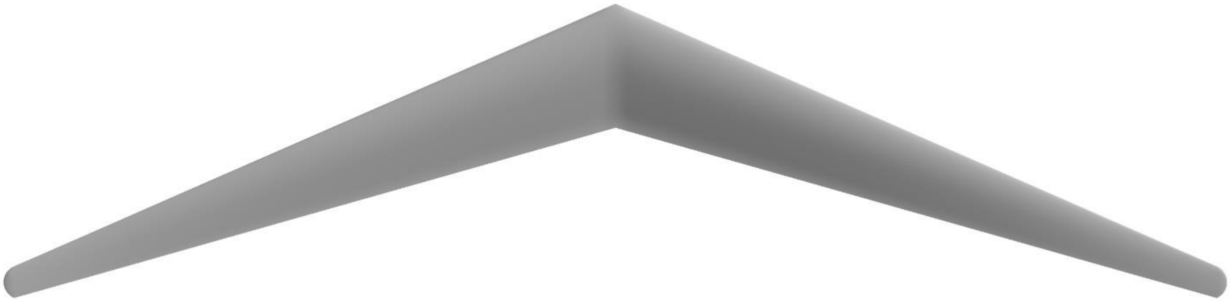

Fig. 2. Model used in simulation.

The P-3C, design by Bowers [7], is based on Prandtl's work on the wing of minimum induced drag published in 1933 [1]. Prandtl's previous work, published in 1921 [11], constrained the wing span and presented the elliptical span load as the configuration of minimum induced drag. However, the work published in 1933 used the wing bending moment as the constraint. His result published in 1933 can be summarized by examining the span load and the downwash angle as a function of semi-spanwise distance. The representative span load and downwash angle per normalized spanwise distance are presented in Fig. 3, taken from Bowers [7]. As shown in Fig. 3, rather than the well known elliptical load [11], the span load is a quadratic function in the shape of a bell. The maximum load is at the symmetry plane while the load and the slope of the load tapers to zero at the wing tip. Examining the downwash angle shown in Fig. 3, the downwash becomes upwash at 70.7% spanwise location. Bowers achieves the bell-shape span load on the P-3C by introducing spanwise twist. The twist angle per spanwise station is plotted in Fig. 4, and the data are provided in Table 2. Bowers' work shows that the wing of a bell-shaped span load has 11% less drag and 22% longer span compared to the elliptically loaded wing of the identical structural weight. Bowers also concluded that a wing with the bell-shaped span load produces induced thrust at the wing tip, thus possessing inherent proverse-yaw characteristics without an additional yaw control device such as a rudder. More details are found in Bowers [7].

Table 2. Wing twist distribution along span [7].

Span location, percent	Angle, degrees	Span location, percent	Angle, degrees
0	8.3274	55	7.2592
5	8.5524	60	6.6634
10	8.7259	65	5.9579
15	8.8441	70	5.1362
20	8.903	75	4.1927
25	8.8984	80	3.1253
30	8.8257	85	1.9394
35	8.6801	90	0.6589
40	8.4565	95	-0.6417
45	8.1492	100	-1.6726
50	7.7522		

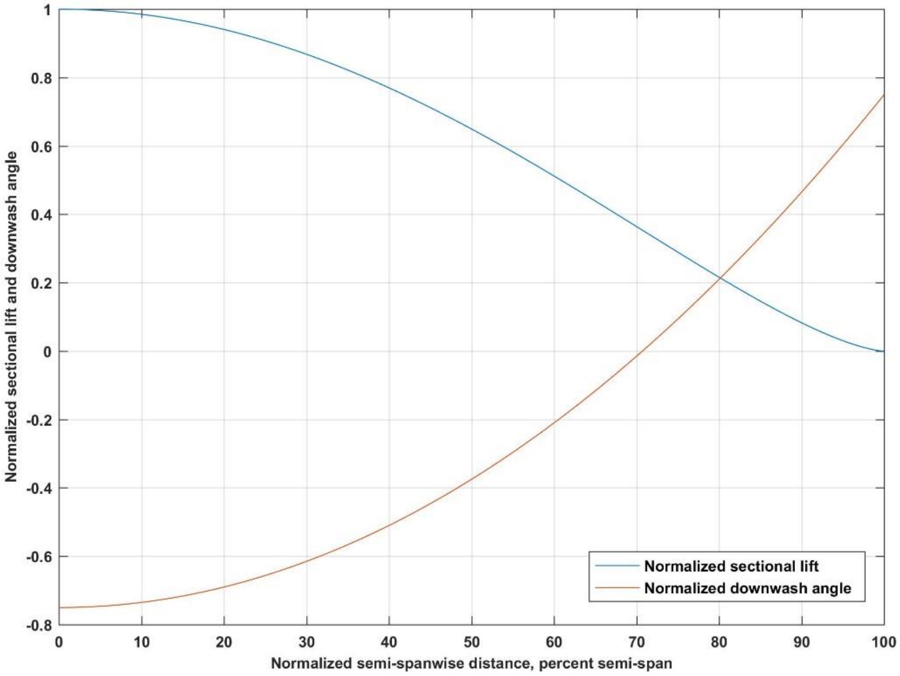

Fig. 3. Prandtl's solution: nondimensionalized sectional lift and downwash angle versus normalized spanwise location, symmetry plane to tip.

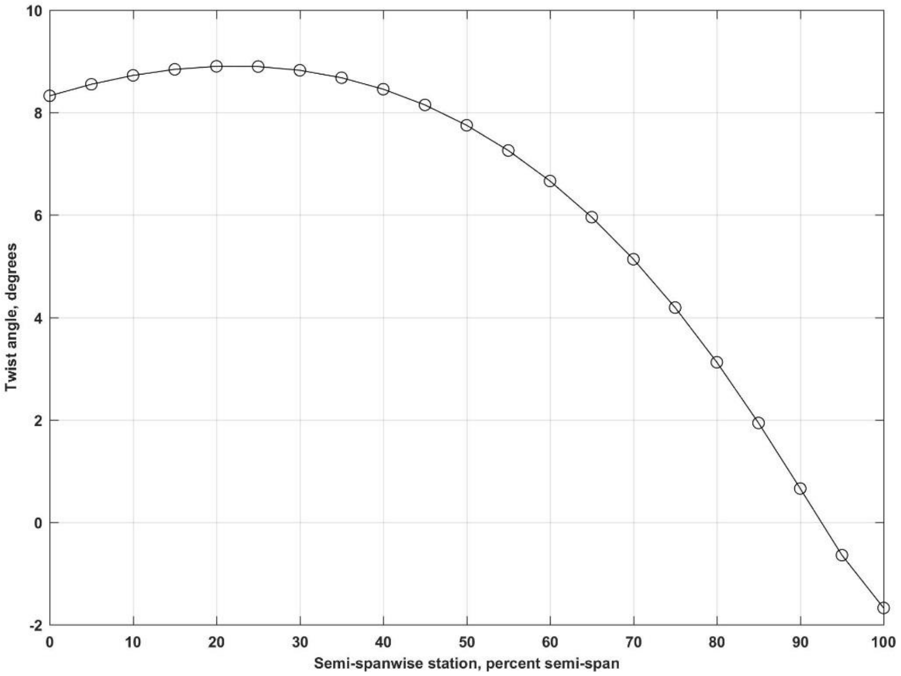

Fig. 4. Twist angle as a function of spanwise station.

IV. Simulation

Simulation conditions and settings are provided in this section. The U.S. standard 1976 atmospheric data were used to define the flight condition. Best practices developed for OVERFLOW were used to create the mesh and perform the simulations.

A. Flight Conditions

All simulations were conducted using the U.S. standard 1976 atmospheric data at an altitude of 2300 ft MSL, the approximate altitude of the Edwards Air Force Base located at Edwards, California. The freestream velocity was 28.79 feet per second, equivalent to Mach 0.026. The atmospheric data and the Reynolds number are tabulated in Table 3. The MAC and the planform area were used as the reference length and reference area, respectively.

Table 3. Atmospheric data.

Variable	Value	Unit
Altitude MSL	2300	ft
Velocity	28.79	ft/s
Density	2.22126E-3	slugs/ft^3
Pressure	1946.15	lbf/ft^2
Temperature	510.468	°R
Speed of sound	1107.59	ft/s
Dynamic viscosity	3.73686E-7	lbf × s/ft^2
Mach number	0.026	
Reynolds number	3.369E5	

B. Flow Solver

Simulations were conducted via CFD, solving the RANS equation using OVERFLOW version 2.2*l* [8]. OVERFLOW is a three dimensional, finite-difference flow solver that specializes in utilizing structured overset grids. Validated for a wide range of flow regime, the results produced using OVERFLOW are submitted regularly to the NASA sponsored workshops such as the AIAA High Lift Prediction Workshop [2-4] . OVERFLOW is capable of employing various numerical schemes, convergence acceleration schemes, turbulence models, and boundary conditions. OVERFLOW also has the capability to automatically generate off-body Cartesian meshes.

In order to produce accurate and reliable results, best practices [9, 10] were utilized with some adjustments. The second order central differencing scheme was used to discretize the governing equation and solved using the Beam-Warming scalar pentadiagonal scheme. The low Mach number preconditioning scheme was utilized due to the low Mach number of 0.026. Second and fourth order dissipation schemes were employed to eliminate spurious oscillations and stabilize the solution. The local time stepping scheme was used to resolve the flow in time. The Spalart-Allmaras turbulence model with rotation and curvature correction [12] with the fully turbulent flow assumption was used to model turbulence.

It is noted that the Reynolds number of 3.369E5 may be low for the fully turbulent approximation. However, private conversations with the designer of the wing, Bowers [7], revealed that, although the Reynolds number is low, turbulent flow would exist in the pressure recovery of the airfoil. As such, it was not anticipated that laminar separation would be an issue and turbulent separation was anticipated near stall. Separate analysis done by the designer showed that at high angle-of-attack conditions, approximately 60% of the upper surface at the symmetry plane was turbulent, and flow over the wing was transitional flow, rather than laminar. As such, the fully turbulent flow assumption was acceptable for the study.

As best practices suggest, the angle-of-attack (AoA) ramp-up procedure was employed to minimize numerical hysteresis in solutions [10]. This study used the procedure developed by Bui [5, 6] which was utilized to accurately simulate and predict flow of the modified Gulfstream G-III at high angle of attack. The procdure was also used to simulate the trapezoidal wing configuration used in the first AIAA High Lift Prediction Workshop [5]. The procedure is outlined below:

1) Run simulations, starting from the freestream initial condition, at an AoA of -4° to 18° using ΔAoA of 2°.
2) Find the stall angle ($\mathrm{AoA}_{\mathrm{stall}}$).
3) Compute a new ΔAoA by scaling the current ΔAoA by 0.5.
4) Restart from the AoA that is one ΔAoA lower than $\mathrm{AoA}_{\mathrm{stall}}$ using the new ΔAoA computed in step 3.
5) Continue to proceed through the AoA in a sequential manner, restarting from a converged solution of lower AoA, using ΔAoA computed in step 3, until stall is detected.
6) Repeat step 2 through step 5 until the desired ΔAoA resolution has been achieved.

This study refined the $\mathrm{AoA}_{\mathrm{stall}}$ to 0.25°. The solution was deemed converged when the standard deviation of the lift, drag, and pitching moment coefficient were 1e-4 or smaller for the final 2000 iterations. The residual values were also monitored to ensure that all residual values were below 1e-6.

C. Mesh Generation

To fully utilize the capabilities of the flow solver, structured overset grids were generated to discretize the geometry and the flow domain. Structured overset grids can be divided into two separate regions: near field and far field. The near field grids were generated as a set of overlapping body-fitted generalized curvilinear grids and the far field grids as a set of overlapping Cartesian grids.

The Chimera Grid Tools (CGT) [13] was used to generate the near field grids using the best practices developed [9, 10]. Grids were generated with a minimum of a 5-point overlap between grids for second order interpolation in the overlapping regions. A minimum of 5 points was placed on all surfaces. The volume grids were generated using the hyperbolic marching scheme [14], using y+ value of 1.0 or lower based on the grid resolution being simulated for the grid independence study. The first 6 cells off of the surface were generated with constant grid spacing. The hyperbolic marching distance was fixed to 10 inches. A maximum stretching ratio of surface grids and volume grids was fixed to 1.3 or lower for higher resolution grids created for the grid independence study.

The far field grids were generated utilizing the automated far field Cartesian mesh generation capability of OVERFLOW. The automated mesh generation capability requires user-supplied near field grids and automatically generates a series of overlapping Cartesian grids of uniform spacing until the specified far field distance has been reached. The spacing of the Cartesian grids differs based on the level of the grid; level-1 being the grids enclosing the supplied near field grids and level-N being the grids that are at the far field distance. The grid spacing doubles from level-i to level-i+1. The user can control the rate at which the Cartesian grid expands to far field via a variable called MINBUF which determines the minimum number of points at each grid level before switching to the next-coarser grid level [8]. The far field distance was fixed to 125 ft which is approximately 63 times the MAC. The representative near body grid is presented in Fig. 5.

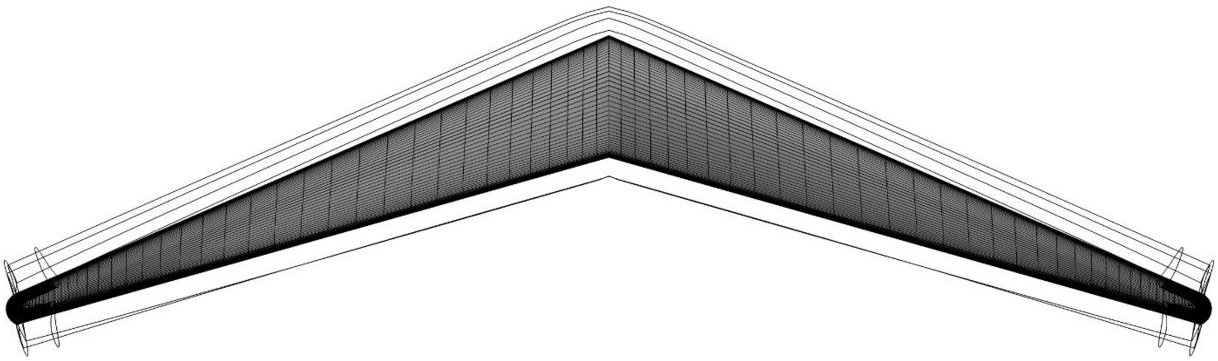

Fig. 5. Representative near body surface with near body volume grid outline.

V. Results

Results of the grid independence study and flow analysis are provided. The grid independence study shows adequate resolution has been achieved for the study. The flow analysis shows that stall occurs at 17.25°. Flow visualizations of the upper and lower surface of the wing show that flow at the wing tip remains attached for all AoA simulated.

A. Grid Independence Study

A grid independence study is an important fundamental study to CFD analysis as it identifies the effect of discretization error. Based on the grid density distribution and resolution, the solution can change as the grid may lack resolution on the surface or in the regions to resolve the flow physics with sufficient accuracy. Lift, drag, and pitching moment coefficients were analyzed to determine whether sufficient resolution has been achieved for the study.

To ease the process of generating grids of multiple resolution in a consistent manner, the grid generation process was automated using the script library of CGT. A total of four grids of different densities were created and simulated: coarse (4.48 mil points), medium (21.9 mil points), fine (79.6 mil points), and finer (190.3 mil points). Parameters used to create different grid densities are summarized in Table 4.

Table 4. Summary of the grid parameters for different grid resolutions.

	Parameter	Coarse	Medium	Fine	Finer
Surface	Stretching ratio	1.3	1.2	1.1	1.05
	Maximum spacing, in	20	10	2.5	2.5
	Minimum spacing, in	0.0157	0.00787	0.00197	0.00197
Volume	Stretching ratio	1.3	1.2	1.1	1.05
	Marching distance, in	10.0			
	Initial spacing off of the wall, in	6.50E-04	1.90E-04	6.45E-05	3.23E-05
	Final spacing off in the near field grid, in	1.0	0.5	0.33	0.25
	y+	1.0	0.3	0.1	0.05
	Level-1 spacing, in	0.8	0.4	0.264	0.2
	MINBUF	4	4	6	8
Total number of grid points (millions)		4.48	21.9	79.6	190.3

The lift coefficient (C_L), drag coefficient (C_D), and pitching moment coefficient (C_m) as a function of AoA of the simulated grids are plotted in Fig. 6, Fig. 7, and Fig. 8, respectively. The AoA_{stall}, C_L at stall (C_{L_stall}), maximum C_L (C_{L_max}), and the respective error relative to the finer grid result are summarized in Table 5. Similarly, the C_D and C_m at AoA_{stall} for different grid resolutions, and the respective errors relative to the finer grid are tabulated in Table 6.

Results show that AoA_{stall} is 17.25°, and the AoA of C_{L_max} is approximately 16° for all resolutions. When comparing the forces and moment coefficients of the two finest levels of the grid resolution, the results show that the largest relative error is -1.39%. Figure 6 and Fig. 7 show that the general trend of C_L and C_D as a function of AoA are identical for all resolutions simulated. Figure 8 shows a drop in C_m at stall which becomes more refined with increasing grid resolution. The C_L, C_D, and C_m shown in Figs. 6-8 as well as consistent AoA_{stall} between different resolutions show that grid independence has been achieved to a level suitable for this study. Solutions present in the rest of the paper refer to the solutions of the finer mesh.

Table 5. Stall angle, stall C_L, Maximum C_L, and error with respect to the finest mesh.

Grid resolution	Stall angle, degrees	C_{L_stall}	C_{L_stall} error, percent	C_{L_max}	C_{L_max} error, percent
Coarse	17.25	1.0106	-3.05	1.0265	2.24
Medium	17.25	1.0216	-1.99	1.0350	1.43
Fine	17.25	1.0378	-0.44	1.0450	0.48
Finer	17.25	1.0424	--	1.0500	--

Table 6. C_D and C_m at stall angle and error with respect to the finest mesh.

Grid resolution	C_{D_stall}	C_{D_stall} error, percent	C_{m_stall}	C_{m_stall} error, percent
Coarse	0.12020	0.08	-0.2050	-7.78
Medium	0.11885	-1.05	-0.2137	-3.87
Fine	0.11968	-0.36	-0.2192	-1.39
Finer	0.12011	--	-0.2223	--

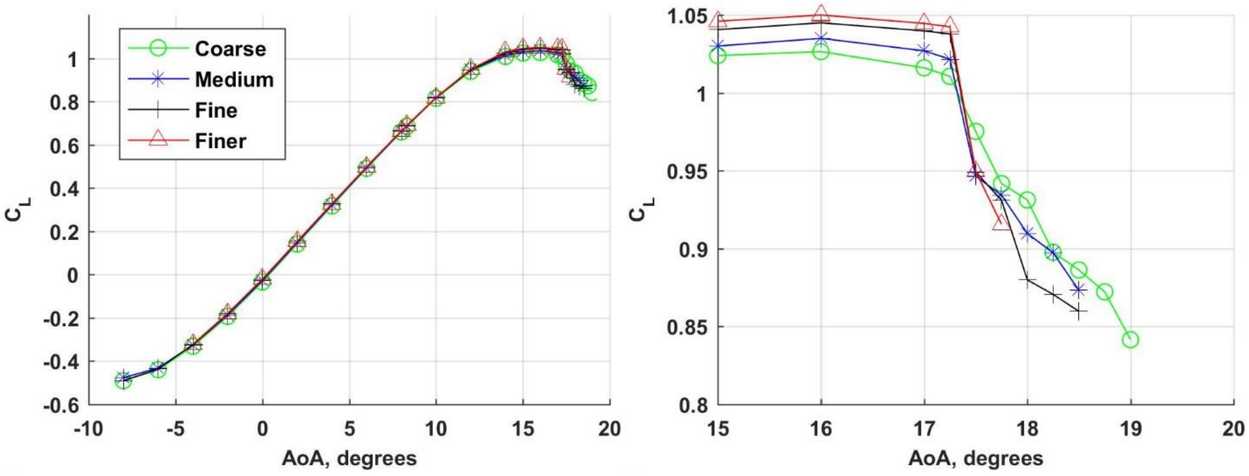

a) C_L for all simulated AoA. **b) Close up view near AoA_{stall}.**

Fig. 6. C_L versus AoA.

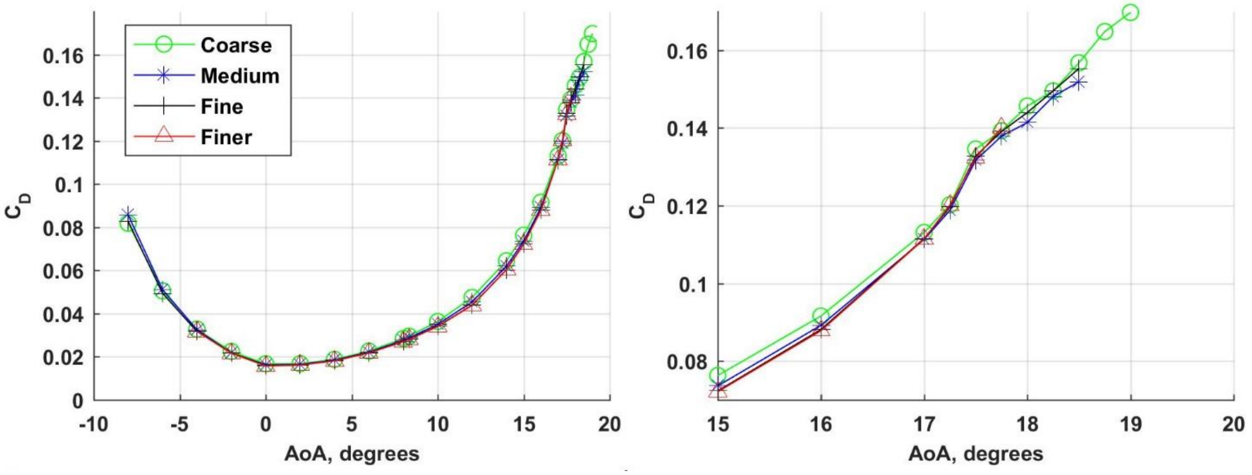

a) C_D for all simulated AoA. **b) Close up view near AoA_{stall}.**

Fig. 7. C_D versus AoA.

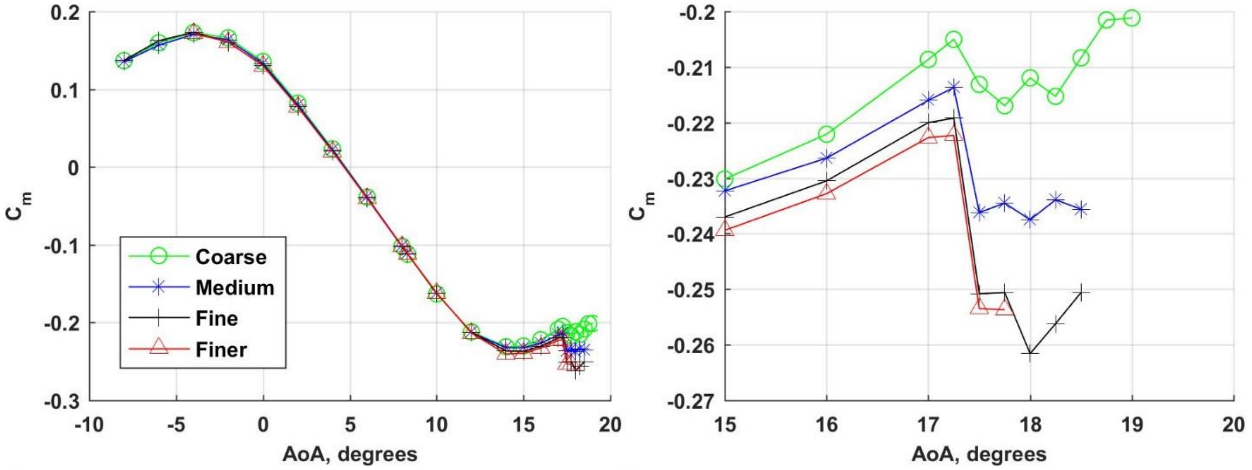

a) C_m for all simulated AoA. **b) Close up view near AoA_{stall}.**

Fig. 8. C_m versus AoA.

B. Stall Analysis

The C_L as a function of angle of attack is plotted in Fig. 9. The result of the bottom surface at 12.0° AoA is shown in Fig. 10. Only one solution of the lower surface is presented because, although the pressure coefficient changed with the AoA as expected, the streamline did not change with the change in the AoA. The surface contour of the pressure coefficient and the surface streamline of the upper surface for selected AoA between 0.0° and 17.50° is presented in Fig. 11.

The results show stall occurring at 17.25° AoA with a sharp break in C_L, shown in Fig. 9. The cause of the loss of C_L can be seen in Fig. 11. The flow separation begins at 8° AoA between the symmetry plane and 60% span. With increasing AoA the separation grows toward the leading edge. At 17.25° AoA the flow is separated for most of the wing, especially at 40% span. It is also shown that, as AoA increases beyond the stall, the separation region grows toward the symmetry plane.

The streamlines shown in Fig. 11 indicate that flow at the wing tip remains attached from low AoA to post-stall AoA. The attached flow observed is due to the spanwise twist of the wing. The tip of the wing is at approximately -10° twist relative to the symmetry plane. Consequently at 17.0° AoA the tip is at approximately 7.0° AoA relative to freestream. Although the large separation region is seen at 17.50° AoA near the symmetry plane, flow becomes increasingly attached as it approaches the wing tip.

More observations on the flow at the wing tip can be made based on the surface pressure coefficient taken at the wing tip (12.3 ft from the symmetry plane), shown in Fig. 12. At 8.00° AoA, the wing tip produces near zero lift as the difference in pressure between the lower surface and the upper surface is negligible. The unloaded wing tip is in line with the design constraint, explained previously, that requires the lift at the wing tip to approach zero. As the AoA diverges from the design condition, the lift generated by the wing tip varies linearly. Examining the surface pressure coefficient at 4.00° and 12.00° AoA, the pressure coefficients are nearly identical; however, the pressure side and the suction side are reversed. Similar observations can be made between 0.00° and 17.25°. The attached flow at the wing tip is in line with a comment made by the pilot of the aircraft during a conversation stating, “the aircraft was totally controllable at high angle of attack.”

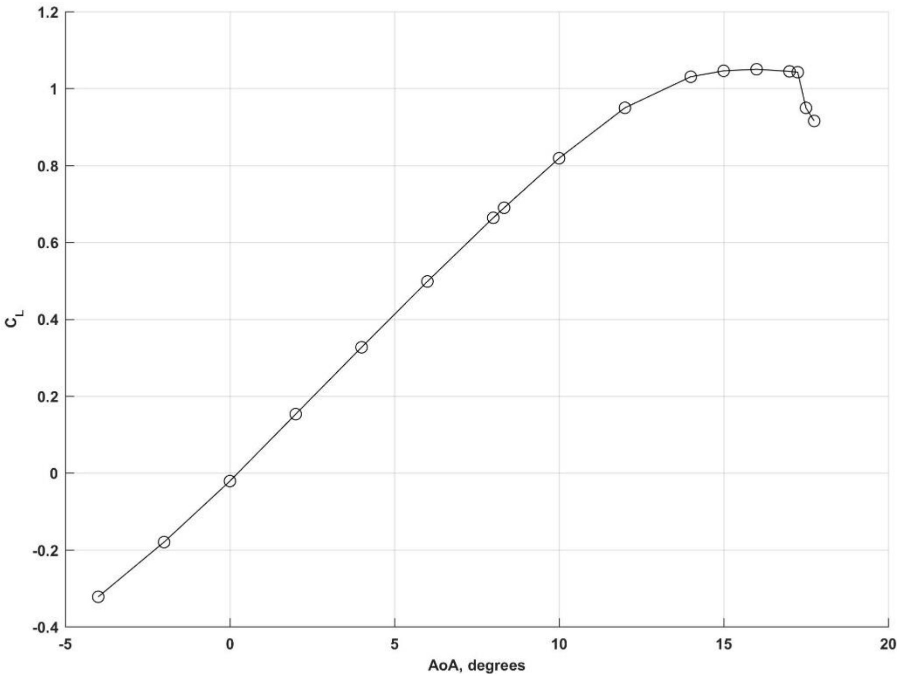

Fig. 9. C_L versus AoA.

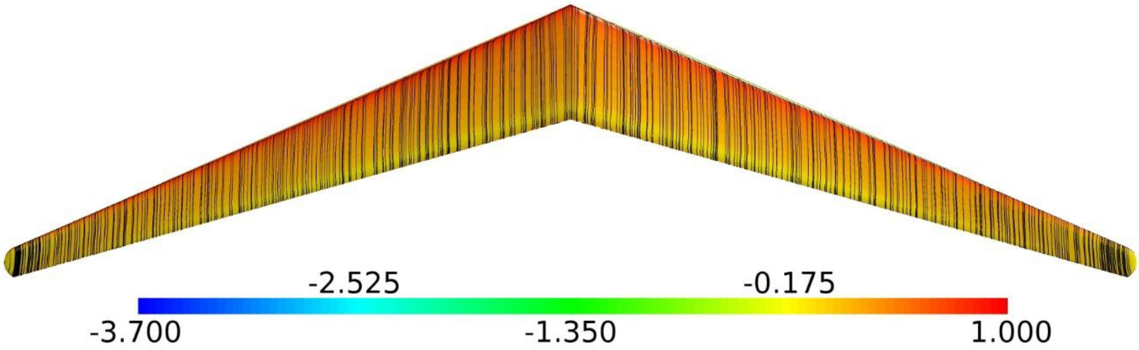

Fig. 10. Pressure coefficient contours and surface streamlines of the lower surface at 12.0° AoA.

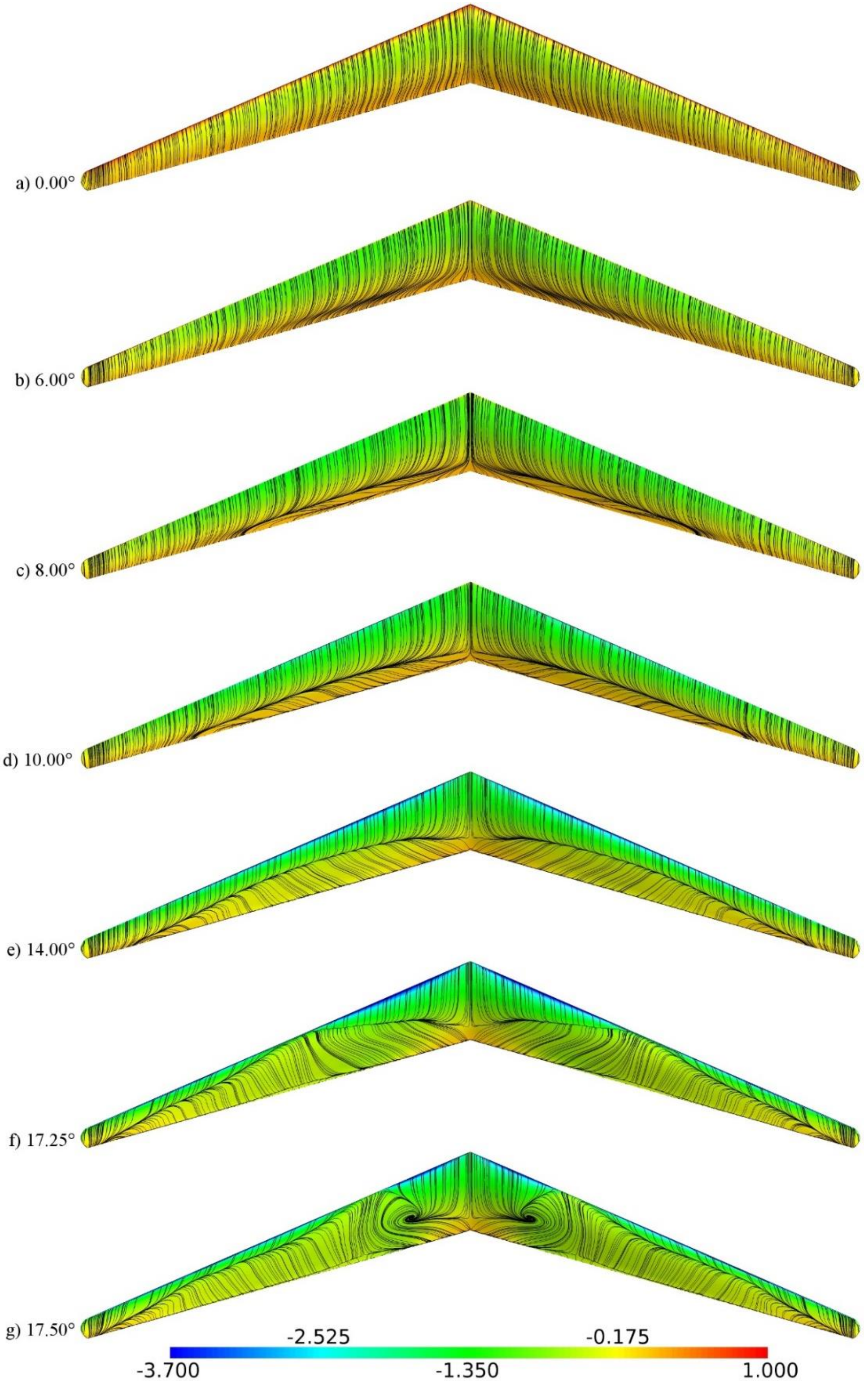

Fig. 11. Pressure coefficient contours and surface streamlines of the upper surface selected AoA.

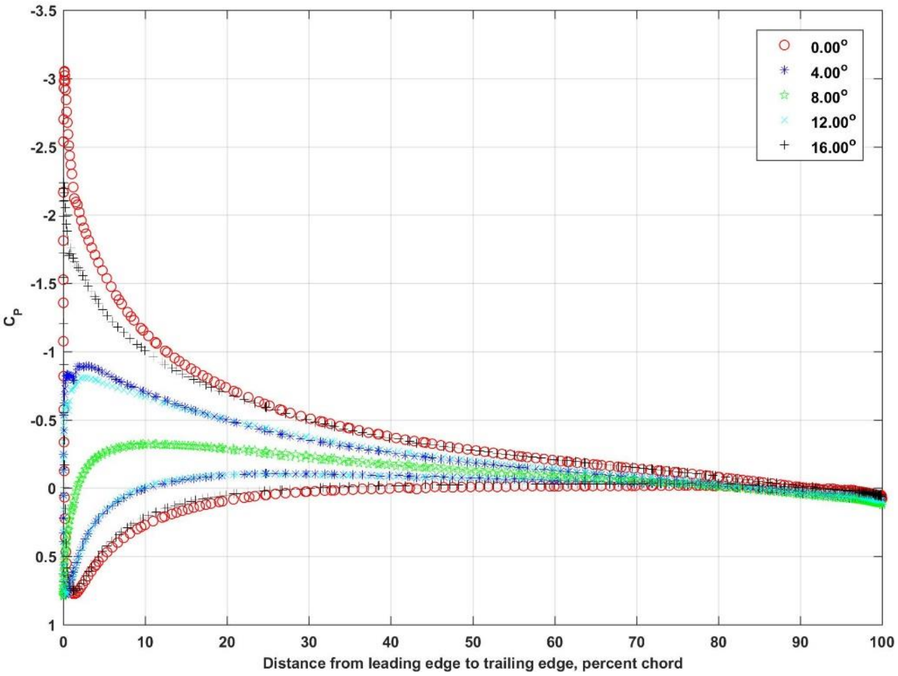

Fig. 12. Pressure coefficient at 100% span for various AoA.

VI. Conclusion

Stall analysis of a wing design based on Prandtl's minimum induced drag theory along with a detailed grid independence study was presented. The results based on the grid independence study show that a suitable level of grid resolution has been achieved for both maximum lift coefficient and stall angle. The results show that stall occurs at an angle of attack of 17.25°±0.25°. The results also show that no undesirable lift, drag, and pitching moment behavior are present. Additionally, both surface and sectional pressure coefficients show that, although severe flow separation is present at high angle-of-attack conditions, the flow at the wing tip remains attached for angle of attack from 0.0° to 17.5° which is the range of the angle of attack simulated.

Acknowledgments

The author thanks Albion Bowers at NASA Armstrong Flight Research Center. His insight and experience in designing and operating P-3C has been invaluable.

References

[1] Prandtl, L., "Uber Tragflugel Kleinsten Induzierten Widerstandes," Zeitschrift fur Flugtecknik und Motorluftschiffahrt, 28 XII 1933, Munchen, Deustchland.

[2] Slotnick, J. P., Hannon, J. A., and Chaffin, M., "Overview of the First AIAA CFD High Lift Prediction Workshop (Invited)," AIAA-2011-862, 2011.
doi: 10.2514/6.2011-862

[3] Rumsey, C. L., and Slotnick, J. P., "Overview and Summary of the Second AIAA High-Lift Prediction Workshop," *Journal of Aircraft*, Vol. 52, No. 4, 2015, pp. 1006-1025.
doi: 10.2514/1.C032864

[4] Rumsey, C. L., Slotnick, J. P., and Sclafani, A. J., "Overview and Summary of the Third AIAA High Lift Prediction Workshop," AIAA-2018-1258, 2018.
doi: 10.2514/6.2018-1258

[5] Bui, T. T., "Analysis of Stall Aerodynamics of a Swept Wing with Laminar-Flow Glove," *Journal of Aircraft*, Vol. 52, No. 3, 2015, pp. 867-871.
doi: 10.2514/1.C032883

[6] Bui, T. T., "Analysis of Low-Speed Stall Aerodynamics of a Swept Wing with Seamless Flaps," AIAA-2016-3720, 2016.
doi: 10.2514/6.2016-3720

[7] Bowers, A. H., Murillo, O. J., Jensen, R., Eslinger, B., and Gelzer, C., "On Wings of the Minimum Induced Drag: Spanload Implications for Aircraft and Birds," NASA/TP-2016-219072, 2016.

[8] Nichols, R. H., and Buning, P. G., "User's Manual for OVERFLOW 2.2: Version 2.2," NASA Langley Research Center, Hampton, Virginia, August 2010, URL: https://overflow.larc.nasa.gov/home/users-manual-for-overflow-2-2/ [retrieved 18 April 2018].

[9] Chan, W. M., Gomez, R. J. III, Rogers, S. E., and Buning, P. G., "Best Practices in Overset Grid Generation," AIAA-2002-3191, 2002.
doi: 10.2514/6.2002-3191

[10] Sclafani, A. J., Slotnick, J. P., Vassberg, J. C., and Pulliam, T. H., "Extended OVERFLOW Analysis of the NASA Trap Wing Wind Tunnel Model," AIAA-2012-2919, 2012.
doi: 10.2514/6.2012-2919

[11] Prandtl, L., "Applications of Modern Hydrodynamics of Aeronautics," NACA-TR-116, 1923.

[12] Shur, M. L., Strelets, M. K., Travin, A. K., and Spalart, P. R., "Turbulence Modeling in Rotating and Curved Channels: Assessing the Spalart-Shur Correction," *AIAA Journal*, Vol. 38, No. 5, 2000, pp. 784-792.
doi: 10.2514/2.1058

[13] Chan, W. M., Rogers, S. E., Pandya, S. A., Kao, D. L., Buning, P. G., Meakin, R. L., Boger, D. A., and Nash, S. M, "Chimera Grid Tools User's Manual: Version 2.1," NASA, March 2010, URL: https://www.nas.nasa.gov/publications/software/docs/chimera/index.html [retrieved 17 April 2018].

[14] Chan, W. M., Chiu, I. T., and Buning, P. G., "User's Manual for the HYPGEN Hyperbolic Grid Generator and the HGUI Graphical User Interface," NASA-TM-108791, 1993.